Inorganic Chemistry

Article

pubs.acs.org/IC

Dopant Concentration–Porosity–Li-Ion Conductivity Relationship in Garnet-Type $Li_{5+2x}La_3Ta_{2-x}Y_xO_{12}$ ($0.05 \leq x \leq 0.75$) and Their Stability in Water and 1 M LiCl

Sumaletha Narayanan, Farshid Ramezanipour,† and Venkataraman Thangadurai*

Department of Chemistry, University of Calgary, 2500 University Dr. NW, Calgary, AB, Canada T2N 1N4

ABSTRACT: Highly Li-ion conductive Y-doped garnet-type $Li_{5+2x}La_3Ta_{2-x}Y_xO_{12}$ ($0.05 \leq x \leq 0.75$) were studied to understand the effects of yttrium- and lithium-doping on crystal structure, porosity, and Li-ion conductivity using ^{7}Li MAS NMR, electrochemical ac impedance spectroscopy, and scanning electron microscopy (SEM), as well as ex situ and in situ powder X-ray diffraction (PXRD) to further explore the potential application of garnets in all-solid-state Li-ion batteries. Solid-state ^{7}Li MAS NMR studies showed an increase in the Li-ion mobility as a function of Y- and Li-doping in $Li_{5+2x}La_3Ta_{2-x}Y_xO_{12}$, which is consistent with the results from ac impedance spectroscopy. The SEM studies on sintered pellets indicated a systematic decrease in porosity and an increase in sinterability as the Y- and Li-doping levels increase in $Li_{5+2x}La_3Ta_{2-x}Y_xO_{12}$. These results are consistent with the calculated porosity and densities using the Archimedes method. Using the variable-temperature in situ PXRD in the temperature range of 30–700 °C, a thermal expansion coefficient of 7.25×10^{-6} K^{-1} was observed for $Li_6La_3Ta_{1.5}Y_{0.5}O_{12}$. To further explore the possibility of a new application for the Li-stuffed garnets, the stability of these materials in aqueous LiCl solution was also studied. A high degree of structural stability was observed in these materials upon 1 M LiCl treatment, making them suitable candidates for further studies as protective layers for lithium electrodes in aqueous lithium batteries.

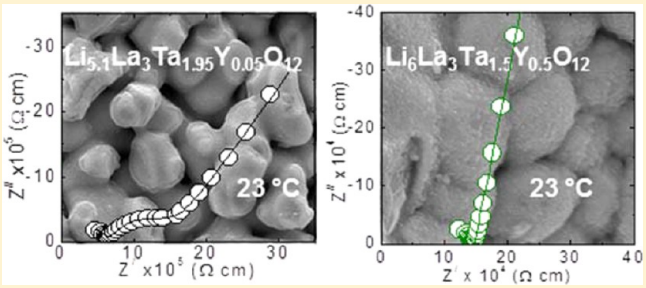

1. INTRODUCTION

The study of lithium-ion conductivity in solid-state materials is motivated by the development of all-solid-state batteries, where the liquid electrolytes are replaced by Li-ion conducting solid electrolytes, which can lead to improved safety, stability, and energy density. Recently, the garnet-type Li-stuffed metal oxides have shown excellent potential for application as solid Li-ion electrolytes.[1] Several members of the garnet family have shown high Li-ion conductivity, chemical stability to elemental Li, and a large electrochemical window at room temperature.[2] In addition to solid electrolyte applications, another area where Li-ion conducting solids can be exploited is in lithium–air batteries. Aqueous electrolytes in these batteries need to be separated from the elemental lithium anode to prevent the vigorous reaction with lithium. To protect the lithium electrode, protective layers consisting of Li-ion conducting solids that are stable in contact with water and elemental Li are desired.[3−5]

The first reported Li-ion conducting garnets, $Li_5La_3M_2O_{12}$ (M = Nb, Ta), showed total Li conductivity (bulk + grain-boundary) of 10^{-6} S cm^{-1} at room temperature.[6] The Ta analogue showed better chemical reaction stability toward molten Li metal and a wider voltage window (>6 V) compared to the Nb member.[7] The Li-ion conductivity can be significantly improved by partial substitution at La or M sites.[8−11] Murugan et al. have synthesized (~1230 °C) cubic $Li_7La_3Zr_2O_{12}$ garnet with a conductivity of $\sim 10^{-4}$ S cm^{-1} at room temperature, which shows good stability toward metallic Li, and therefore, it has been widely studied for all-solid-state Li-ion batteries.[12] However, $Li_7La_3Zr_2O_{12}$ crystallizes in tetragonal geometry when the synthesis temperature is lowered to 980 °C, which possesses 2 orders of magnitude lower conductivity than the cubic phase.[13] Hence, it is important to stabilize the cubic phase of garnets to achieve promising Li-ion conductivity, and dopants such as Al, Ta, Nb, and Y have proven to help to achieve this goal.[14−22] Rangasamy et al. studied the effect of both Li and Al on the $Li_7La_3Zr_2O_{12}$ structure and optimized the amount of Al (0.204 mol.) to stabilize the cubic phase.[16] Substitution of Y, Nb, and Ta led to the improvement of the bulk conductivity of $Li_7La_3Zr_2O_{12}$ from $\sim 10^{-4}$ to $\sim 10^{-3}$ S cm^{-1} at room temperature.[20,22,23] Also, stabilization of the cubic phase at lower temperature (1000 °C) was observed upon Ta substitution at the Zr site in $Li_7La_3Zr_2O_{12}$.[19]

Recently, we showed that the ionic conductivity of $Li_5La_3Nb_2O_{12}$ can be enhanced by partial doping of Y at the Nb sites, leading to the Li conductivity of up to 10^{-4} S cm^{-1} at room temperature.[24] Given the wider voltage window and higher stability of the Ta analogue, $Li_5La_3Ta_2O_{12}$, to metallic lithium, we envisioned the possibility of obtaining high ionic conductivity in the Ta compounds, where both high stability

Received: April 30, 2015
Published: June 30, 2015

DOI: 10.1021/acs.inorgchem.5b00972
Inorg. Chem. 2015, 54, 6968–6977

and Li conductivity can be present. Subsequently, we synthesized and studied the low-temperature dielectric properties of the Y-doped $Li_{5+2x}La_3Ta_{2-x}Y_xO_{12}$ (x = 0.25, 0.5, and 0.75).[25] We showed that the x = 0.5 and 0.75 phases show high conductivity at room temperature, in the order of 10^{-4} S cm^{-1}.[25] Here, we present the detailed study of Y-doped $Li_5La_3Ta_2O_{12}$ phases in a wide temperature range and the trends in their porosity, sinterability, and Li-ion conductivity using ^{7}Li MAS NMR, ac impedance spectroscopy, scanning electron microscopy, and porosity/density measurements. In addition, we show the stability of these materials in aqueous LiCl (1 M) solution, making them potential candidates for application as protective layers for lithium electrodes in lithium aqueous batteries.[3−5]

2. EXPERIMENTAL SECTION

2.1. Sample Preparation of $Li_{5+2x}La_3Ta_{2-x}Y_xO_{12}$ ($0.05 \le x \le 0.75$). The syntheses were performed according to a procedure reported elsewhere.[25] Specifically, desired amounts of $LiNO_3$ (99%, Alfa Aesar), La_2O_3 (99.99%, Alfa Aesar) (preheated at 900 °C for 24 h), Ta_2O_5 (99.5%, Alfa Aesar), and $Y(NO_3)_3$ (99.9%, Alfa Aesar) were thoroughly mixed by ball-milling using 2-propanol, and then they were heated at 700 °C. After the heat treatment, the powder mixture was ball-milled again and pressed into pellets using an isostatic press. The pellets were covered with mother powder in an alumina crucible and were initially heated to 900 °C for 24 h, followed by a final sintering at 1100 °C for 6 h, to ensure the garnet-phase formation.

2.2. Structural and Electrical Analyses of $Li_{5+2x}La_3Ta_{2-x}Y_xO_{12}$ ($0.05 \le x \le 0.75$). The phase analysis was done using powder X-ray diffraction (PXRD) data obtained on a Bruker D8 powder X-ray diffractometer with Cu Kα radiation. Solid-state ^{27}Al and ^{7}Li magic-angle spinning nuclear magnetic resonance (MAS NMR) studies were performed using a spectrometer (AMS 300, Bruker, at a spinning rate of 5 kHz) against solid $Al(NO_3)_3$ and LiCl as standards. The morphological studies were carried out using scanning electron microscopy (SEM) (Philips FEI XL30 and Zeiss Sigma VP). The pellets were cut into small discs using a diamond saw for the SEM analysis. The Archimedes method was used to measure the density of garnets in pellet form using methanol. The ac impedance spectroscopy on the pellets using Au electrodes was carried out on a Solartron SI 1260 impedance and gain-phase analyzer (0.01 Hz to 1 MHz; 100 mV) in an ambient atmosphere.

2.3. Chemical Stability of $Li_{5+2x}La_3Ta_{2-x}Y_xO_{12}$ ($0.05 \le x \le 0.75$) with Respect to Temperature, Water, and LiCl. The structural stability of as-prepared $Li_{5+2x}La_3Ta_{2-x}Y_xO_{12}$ at different temperatures was studied by variable-temperature in situ PXRD using a high-temperature chamber (Anton Paar XRK 900) on the same diffractometer mentioned above. In order to analyze the chemical stability of $Li_{5+2x}La_3Ta_{2-x}Y_xO_{12}$ in water, the powder was stirred in water for 2 days. The stability in aqueous LiCl solution was determined by stirring pellets of $Li_{5+2x}La_3Ta_{2-x}Y_xO_{12}$ in 1 M LiCl for 1 week, after which the pellets were vacuum-dried at ∼100 °C for 6 h prior to the PXRD and conductivity measurements.

3. RESULTS AND DISCUSSION

3.1. Phase Analysis of $Li_{5+2x}La_3Ta_{2-x}Y_xO_{12}$. Rietveld refinements[26,27] with powder X-ray diffraction data were performed to confirm the formation of the garnet-type structure in $Li_{5+2x}La_3Ta_{2-x}Y_xO_{12}$ phases. The results of these analyses for the x = 0.05, 0.1, and 0.2 phases are shown in Table 1, and a typical Rietveld refinement profile, in this case, for x = 0.2 member, $Li_{5.4}La_3Ta_{1.8}Y_{0.2}O_{12}$ is presented in Figure 1. We have recently reported the structural parameters for x = 0.25, 0.5 and 0.75,[25] and hence, it will not be presented for these members in this work. For all $Li_{5+2x}La_3Ta_{2-x}Y_xO_{12}$ ($0.05 \le x \le 0.75$) phases, a cubic structure with space group $Ia\bar{3}d$ can be identified. Because of the larger ionic radius of Y^{3+} (0.90 Å) compared to that of Ta^{5+} (0.64 Å),[28] an increase in the unit cell dimension is expected as the amount of Y^{3+} increases in $Li_{5+2x}La_3Ta_{2-x}Y_xO_{12}$. This increase can be observed from the

Table 1. Rietveld Refinement Results for $Li_{5+2x}La_3Ta_{2-x}Y_xO_{12}$ (x = 0.05−0.20)[a]

	x = 0.05	x = 0.10	x = 0.20
La (24*c*) occupancy	1	1	1
x	1/8	1/8	1/8
y	0	0	0
z	1/4	1/4	1/4
U_{iso}	0.0230(8)	0.0209(7)	0.0224(7)
Ta/Y (16*a*) occupancy	0.975/0.025	0.95/0.05	0.90/0.10
x	0	0	0
y	0	0	0
z	0	0	0
U_{iso}	0.0214(7)	0.0198(6)	0.0206(6)
Li1 (24*d*) occupancy	0.768	0.7453	0.705
x	1/4	1/4	1/4
y	7/8	7/8	7/8
z	0	0	0
U_{iso}	0.025	0.025	0.025
Li2 (48*g*) occupancy	0.156	0.174	0.207
x	1/8	1/8	1/8
y	0.6826	0.6826	0.6826
z	0.5674	0.5674	0.5674
U_{iso}	0.025	0.025	0.025
Li3 (96*h*) occupancy	0.155	0.16	0.1702
x	0.0927	0.0927	0.0927
y	0.684	0.684	0.684
z	0.5795	0.5795	0.5795
U_{iso}	0.025	0.025	0.025
O (96*h*) occupancy	1	1	1
x	0.2896(6)	0.2883(5)	0.2868(5)
y	0.0990(6)	0.1012(5)	0.1012(5)
z	0.19846)	0.1984(6)	0.1996(6)
U_{iso}	0.0207(31)	0.0212(29)	0.0215(28)
R_p (%)	9.18	8.58	8.25
R_{wp} (%)	11.83	11.17	11.01
a (Å)	12.8160(3)	12.8268(4)	12.8642(3)

[a]The Li occupancies are based on the values in ref 4.

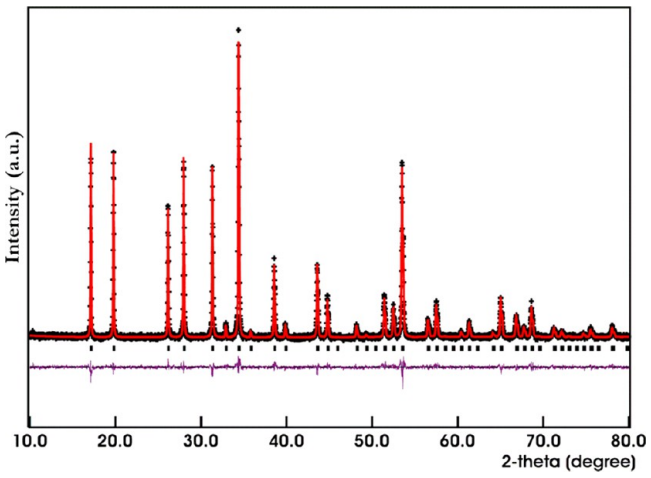

Figure 1. Rietveld refinement profile for $Li_{5.4}La_3Ta_{1.8}Y_{0.2}O_{12}$, indicating the formation of a garnet-type structure.

DOI: 10.1021/acs.inorgchem.5b00972
Inorg. Chem. 2015, 54, 6968−6977

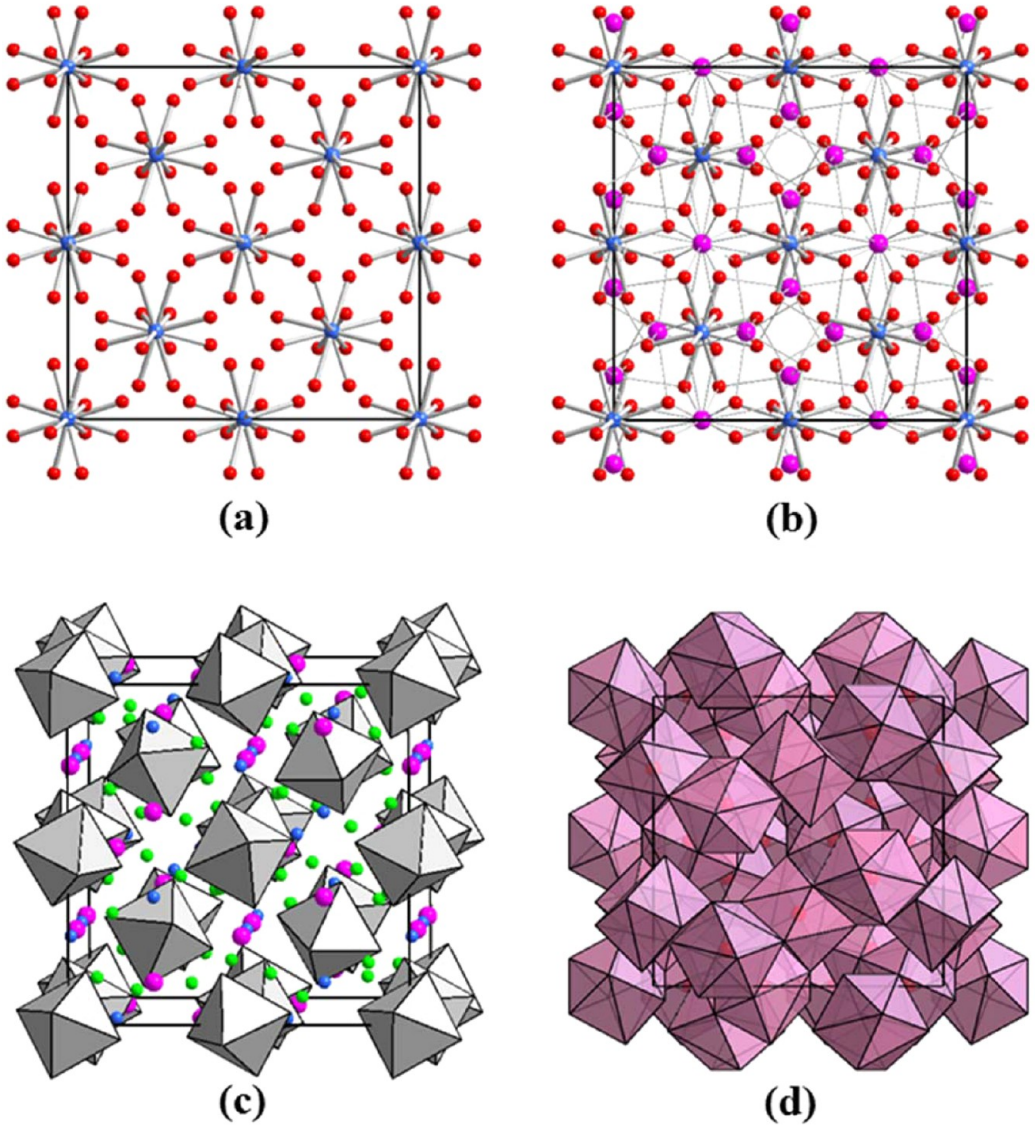

Figure 2. Garnet-type structure of $Li_{5+2x}La_3Ta_{2-x}Y_xO_{12}$. (a) Ta-O sublattice where Ta is shown in blue and oxygen in red. (b) Ta-O sublattice with La (purple) in spaces between TaO_6 units. (c) TaO_6 units shown by gray octahedra. La atoms are in purple, while Li1 (24*d* site) and Li2 (48*g* site) are shown as blue and green spheres, respectively. Li3 (96*h* site) is omitted for clarity. (d) The La-O sublattice showing LaO_8 polyhedra.

data shown in Table 1. In the garnet-type structure, the transition metals (Ta or Y) are octahedrally coordinated by oxygen atoms (Figure 2a). The $Ta(Y)O_6$ octahedra are not connected to each other and do not share corners or edges, unlike in the perovskite-type structure.[29] The La and Li atoms reside in the spaces in between these octahedra. The coordination sphere of La consists of eight oxygen atoms, forming a dodecahedral geometry with triangular faces around the La atom (Figure 2d).

The Li-ion sites in Li-stuffed garnets are well-established in the literature,[10,14,25,30−32] but given the essential role of Li distribution in Li-ion conductivity, some remarks are given in this work. Three crystallographically distinct Li positions are known for this structure type.[30,31] Li(1) is located at the center of a tetrahedron formed by oxygen atoms (24*d* site in Figure 3a), while Li(2) is at the center of an octahedron (48*g* site). Some of the Li atoms are shifted from the centers of the 48*g* site octahedra, leading to new crystallographic positions, 96*h*, for Li(3). Note that the octahedra are connected to the tetrahedra through face-sharing. There is also edge-sharing between neighboring octahedra, as seen in Figure 3. The above arrangement leads to an array of Li atoms surrounded by octahedral or tetrahedral geometry, which form a three-dimensional network throughout the material (Figure 3b), leading to the high Li-ion conductivity observed in these systems. It is important to note that all of the sites shown in Figure 3 cannot be occupied simultaneously due to short Li−Li contacts.[24] An octahedral site will remain vacant if both tetrahedral sites adjacent to it are occupied.[31,32] While the occupancy of Li positions cannot be determined by laboratory PXRD, it is possible to obtain an estimate of the Li occupancy on each site based on the neutron diffraction data on similar materials. O'Callaghan and Cussen have studied $Li_{5+x}Ba_xLa_{3-x}Ta_2O_{12}$ (x = 0, 0.5, 1, 1.2, 1.4, 1.6) and have shown a correlation between the total Li content in the system and the occupancy of Li on each of the three sites, 24*d*, 48*g*, and 96*h*.[31] On the basis of their neutron diffraction data, there is an increase in the Li occupancy on the octahedral sites, 48*g* and

DOI: 10.1021/acs.inorgchem.5b00972
Inorg. Chem. 2015, 54, 6968−6977

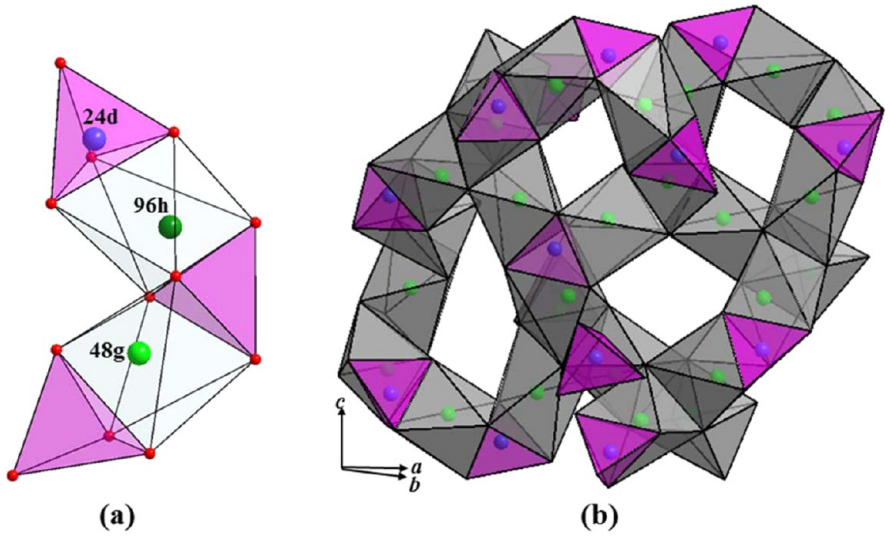

Figure 3. (a) The tetrahedral and octahedral arrangements of oxygen atoms that accommodate the Li atoms. Oxygen atoms are shown as small red spheres at the corners of polyhedra. The Li atoms at the centers of tetrahedra (24*d* site) and octahedra (48*g* site) are shown in blue and light green, respectively. The Li atom that is shifted from the center of the octahedron (96*h* site) is shown in dark green. (b) Three-dimensional connectivity of oxygen octahedra and tetrahedra, which can accommodate Li atoms, shown as blue and green spheres. In the actual structure, not all of the neighboring sites can be simultaneously occupied by Li and it is not possible for a Li atom to exist at an octahedral site if both tetrahedral sites adjacent to it are occupied.

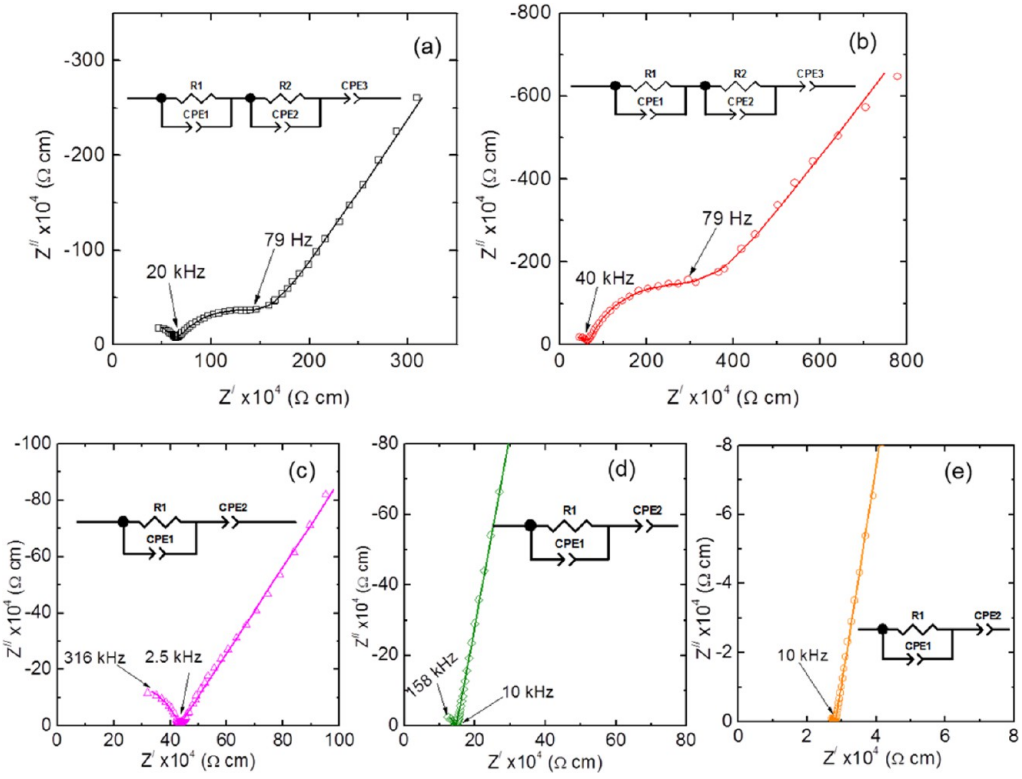

Figure 4. Typical ac impedance plots at 23 °C for $Li_{5+2x}La_3Ta_{2-x}Y_xO_{12}$ ($0.05 \leq x \leq 0.5$): (a) $x = 0.05$, (b) $x = 0.10$, (c) $x = 0.20$, (d) $x = 0.25$, and (e) $x = 0.50$. The open symbols represent the collected data, and the solid lines represent the fitting. The inset figures indicate the equivalent circuits used for fitting analysis.

especially 96*h*, as a function of total Li content. On the other hand, the Li occupancy on the 24*d* site (centers of tetrahedra) decreases as the total Li content increases in Li-stuffed garnets.[1,2] The above information was used to estimate the Li occupancy on each site in our $Li_{5+2x}La_3Ta_{2-x}Y_xO_{12}$ phases, as shown in Table 1. A mechanism for Li conduction has also been proposed before,[20,25] which relies primarily on the Li-hopping between the octahedral sites, implying that greater Li mobility should be associated with higher octahedral site occupancy.

3.2. Li-Ion Conductivity as a Function of Y-Doping and Temperature. The remarkable room-temperature

DOI: 10.1021/acs.inorgchem.5b00972
Inorg. Chem. 2015, 54, 6968−6977

Table 2. AC Impedance Fitting Results of $Li_{5+2x}La_3Ta_{2-x}Y_xO_{12}$ (x = 0.05 and 0.10)

x	R_b (Ω)	CPE_b (F)	n_b	C_b (F)	R_{gb} (Ω)	CPE_{gb} (F)	n_{gb}	C_{gb} (F)	CPE_{el} (F)	χ^2
0.05	1.69×10^4	5.70×10^{-10}	0.76	1.37×10^{-11}	2.18×10^4	1.59×10^{-7}	0.74	2.07×10^{-8}	3.33×10^{-6}	0.0002
0.10	1.49×10^4	1.40×10^{-9}	0.71	1.55×10^{-11}	4.84×10^4	3.34×10^{-8}	0.87	1.32×10^{-8}	9.05×10^{-7}	0.0003

Table 3. Room-Temperature ac Impedance Fitting Results of $Li_{5+2x}La_3Ta_{2-x}Y_xO_{12}$ (x = 0.20, 0.25, and 0.50)

x	R_b (Ω)	CPE_b (F)	n_b	C_b (F)	CPE_{el} (F)	χ^2
0.20	2.00×10^4	2.83×10^{-9}	0.79	1.12×10^{-11}	6.74×10^{-6}	0.0008
0.25	8.89×10^4	1.77×10^{-9}	0.67	8.06×10^{-12}	3.24×10^{-6}	0.0008
0.50	2.26×10^4	8.48×10^{-9}	0.57	2.10×10^{-12}	3.00×10^{-6}	0.0001

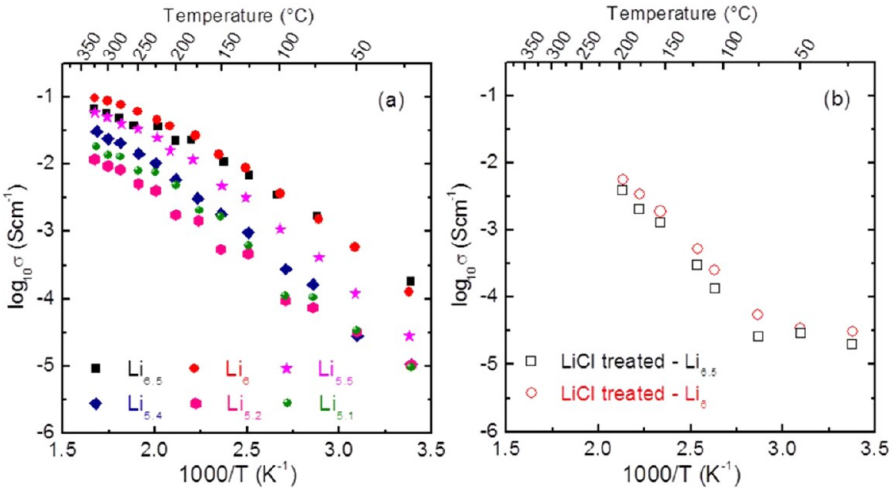

Figure 5. Arrhenius plots showing the conductivity variation against temperature of (a) as-prepared $Li_{5+2x}La_3Ta_{2-x}Y_xO_{12}$ ($0.05 \le x \le 0.75$) and (b) $Li_{5+2x}La_3Ta_{2-x}Y_xO_{12}$ (x = 0.5, and 0.75) after treatment with 1 M LiCl solution.

conductivity of the x = 0.5 and 0.75 phases of $Li_{5+2x}La_3Ta_{2-x}Y_xO_{12}$, ~$10^{-4}$ S cm^{-1},[25] prompted us to study the conductivity over a much wider temperature range of 23−325 °C and look at the conductivity trends as a function of doping and temperature for the entire series from x = 0.05 to x = 0.75. In addition, we show the dependence of the Li-ion mobility on Li content using ^{7}Li MAS NMR spectroscopy. Typical ac impedance data of $Li_{5+2x}La_3Ta_{2-x}Y_xO_{12}$ (x = 0.05−0.5) recorded at room temperature are shown in Figure 4. They show one or two semicircles at the high-frequency side and a spike at the low-frequency side. This behavior is typical for Li-stuffed garnet-type solid Li-ion electrolytes.[6,7,33] The data are fitted using an equivalent circuit of resistances and constant phase elements (CPEs), which are shown as insets in Figure 4. The open symbols and the solid lines represent the measured and fitted data, respectively. The equivalent circuits represent the contributions from the electrical bulk, grain-boundary, and electrode responses. The capacitance (C) value is calculated according to eq 1

$$C = R^{((1-n)/n)}\mathrm{CPE}^{(1/n)} \quad (1)$$

where R, CPE, and n represent the resistance, constant phase element, and fitting parameter. The lower doped $Li_{5+2x}La_3Ta_{2-x}Y_xO_{12}$ (x = 0.05 and 0.10) were fitted using the equivalent circuits comprising two sets of parallel R and CPE components and a series CPE component compared to the higher doped $Li_{5+2x}La_3Ta_{2-x}Y_xO_{12}$ (x = 0.20−0.5), where only one set of R and CPE parallel circuit was used. The calculated bulk (C_b) and grain-boundary (C_{gb}) capacitance are in the range of 10^{-11}−10^{-12} and 10^{-8} F, respectively, which are in agreement with values expected for these materials (Tables 2 and 3).[34] The goodness of fit is indicated by χ^2, where lower χ^2 indicates greater reliability of the fit. In all cases, very low χ^2 values, in the order of 10^{-4}, were obtained, indicating excellent fits.

The results of the electrical conductivity studies at the temperature range of 23−325 °C are given in the Arrhenius plots (Figure 5a). As the temperature increases, the total (bulk + grain-boundary) conductivity increases as expected for garnet-type materials. In addition, the conductivity increases with increase in Li content and Y-doping, confirming once again that Li stuffing helps to increase the ionic conductivity in garnets.[24,35] A decrease in activation energy from 0.43 to 0.33 eV (calculated at 23−325 °C) was observed with the increase in x in $Li_{5+2x}La_3Ta_{2-x}Y_xO_{12}$, as shown in Table 4 along with the total conductivity values at 23 °C. Note that activation

Table 4. Room-Temperature (23 °C) Conductivity and Activation Energies of $Li_{5+2x}La_3Ta_{2-x}Y_xO_{12}$ Calculated at 23−325 °C[a]

x in $Li_{5+2x}La_3Ta_{2-x}Y_xO_{12}$	$\sigma_{23\ °C}$ (S cm^{-1})	E_a (eV)
0.05	9.56×10^{-6}	0.43
0.10	1.04×10^{-5}	0.40
0.20	1.07×10^{-5}	0.44
0.25	2.82×10^{-5}	0.43
0.50	1.26×10^{-4}	0.37
0.75	1.83×10^{-4}	0.33

[a]We have reported the conductivity values for x = 0.25, 0.5, and 0.75 before.[25] These values are repeated here to show the trend.

DOI: 10.1021/acs.inorgchem.5b00972
Inorg. Chem. 2015, 54, 6968−6977

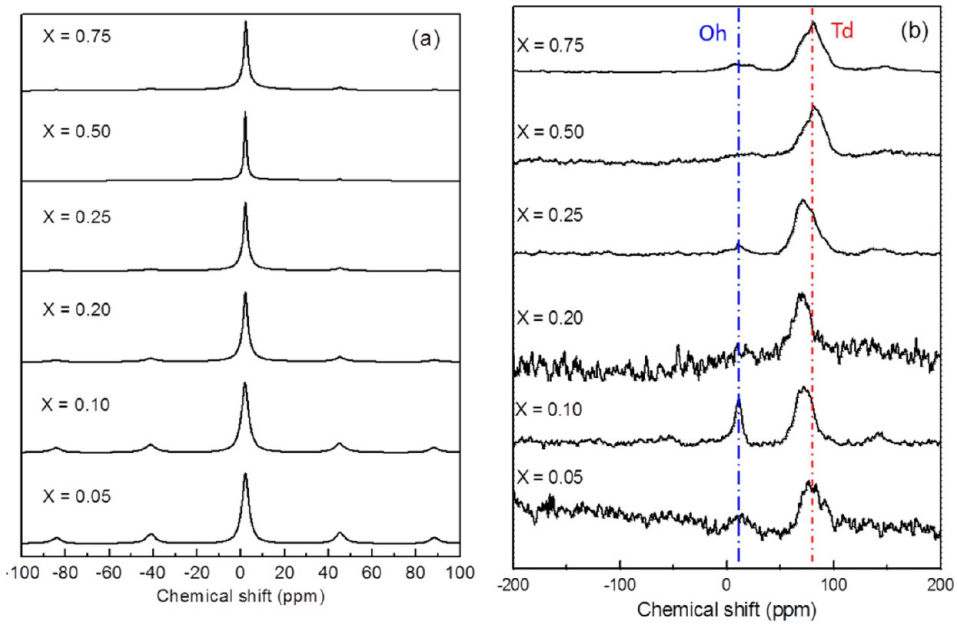

Figure 6. (a) ^{7}Li and (b) ^{27}Al MAS NMR of $Li_{5+2x}La_3Ta_{2-x}Y_xO_{12}$ ($0.05 \leq x \leq 0.75$). Chemical shift was measured against solid LiCl for ^{7}Li MAS, and $Al(NO_3)_3$ for ^{27}Al MAS NMR. A spinning frequency of 5 kHz was used.

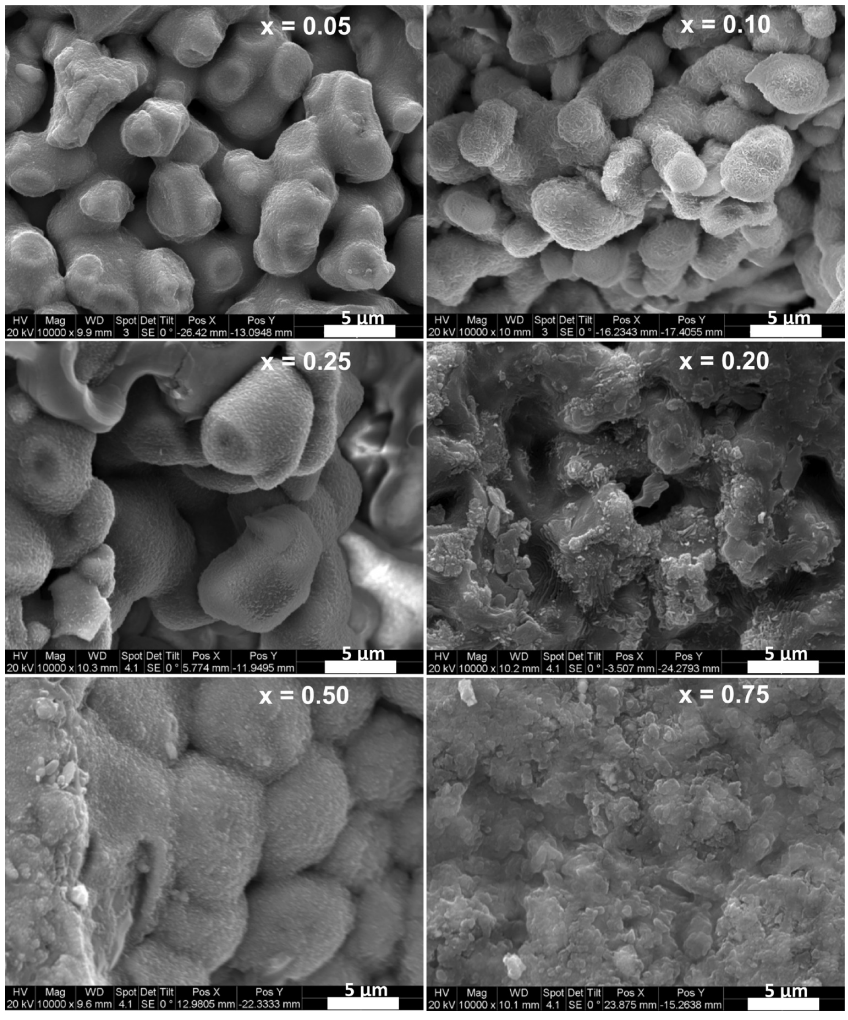

Figure 7. Morphological studies of $Li_{5+2x}La_3Ta_{2-x}Y_xO_{12}$ (x = 0.05−0.75) pellets using SEM microscopy.

DOI: 10.1021/acs.inorgchem.5b00972
Inorg. Chem. 2015, 54, 6968−6977

energies from the data at a wide temperature range (23−325 °C) are generally smaller than those reported before for the x = 0.25, 0.5, and 0.75 using the low-temperature data from −50 to 50 °C.[25]

The conductivity trend as a function of Li content is also consistent with the results of the ^{7}Li magic-angle spinning NMR studies. Figure 6a shows the ^{7}Li MAS NMR data, which are expressed against the chemical shift value of solid LiCl. A characteristic single peak near 0 ppm is observed and is the typical behavior of garnet-type compounds.[36,37] As the Y-doping and the Li content increase, the peak becomes narrower, indicating faster mobility of Li, and confirming that the Li-ion mobility is enhanced as a function of lithium content in the materials.

In addition, we were interested in verifying if our materials contained any Al, because there have been reports of the inclusion of Al from the alumina crucible into another garnet, $Li_7La_3Zr_2O_{12}$, during sintering, which appeared to stabilize the cubic structure versus tetragonal in that material.[14,17] Therefore, ^{27}Al magic-angle spinning (MAS) NMR measurements were performed on all samples and indicated the presence of Al in $Li_{5+2x}La_3Ta_{2-x}Y_xO_{12}$ ($0.05 \le x \le 0.75$). As seen in Figure 6b, there are two peaks in the ^{27}Al MAS NMR data. The peak appearing in the range of 10−15 ppm represents octahedrally coordinated Al and has been proposed previously to correspond to small amounts of $LaAlO_3$.[8] However, recently, it has been shown that Al originating from the alumina crucible can be included in the garnet structure by residing on the octahedral 48*g* site and sharing that site with lithium.[15] The ^{27}Al MAS NMR peaks appearing in the range of 70−80 ppm correspond to Al in 4-fold coordination based on the chemical shift.[8] It has been suggested previously that these four-coordinated Al atoms are located in some of the 24*d* tetrahedral sites in the garnet structure, sharing that site with lithium.[14,17] Therefore, the ^{27}Al MAS NMR data indicate the inclusion of trace amounts of aluminum in our materials. However, it is unclear if this Al inclusion plays any role in the stabilization of the cubic structure in the investigated garnet phases.

3.3. Trends in Porosity and Sinterabiliy as a Function of Y-Doping. Using scanning electron microscopy (SEM) and porosity/density calculations, a correlation has been established between the Y (and Li) content and the sinterability of $Li_{5+2x}La_3Ta_{2-x}Y_xO_{12}$ ($0.05 \le x \le 0.75$). The scanning electron micrographs for $Li_{5+2x}La_3Ta_{2-x}Y_xO_{12}$ are shown in Figure 7. As seen here, a high degree of porosity is present in the sintered pellets of materials that have a smaller degree of doping, while the pellets become considerably denser upon increasing the Y (and Li) content. The SEM results are also qualitatively consistent with the percent-porosity values (Table 5) obtained based on Archimedes principle. The porosity of the samples can be calculated using the formula[38]

Table 5. Calculated and Measured Density Results of $Li_{5+2x}La_3Ta_{2-x}Y_xO_{12}$ from PXRD and Archimedes Methods

x in $Li_{5+2x}La_3Ta_{2-x}Y_xO_{12}$	measured density (g cm^{-3})	theoretical density (g cm^{-3})	Archimedes porosity (%)
0.05	3.463	6.320	29
0.10	3.114	6.279	35
0.20	3.353	6.176	30
0.25	3.479	6.104	28
0.50	4.919	5.928	0.5
0.75	4.776	5.772	1.6

$$\%\ \text{porosity} = \left(\frac{W_{Sat} - W_{Dry}}{W_{Sat} - W_{Susp}}\right) \times 100 \quad (2)$$

where W_{Sat}, W_{Dry}, and W_{Susp} indicate the saturated, dry, and suspended weights, respectively. The porosities of sintered pellets for x = 0.05, 0.1, 0.2, and 0.25 are close to each other and ranges between 28% and 35%. However, there is a significant decrease in porosity for x = 0.5 and 0.75, where the calculated porosities are about 0.5% and 1.6%, respectively. These results are found to be consistent with the densities of sintered pellets (Table 5) obtained using the Archimedes method based on eq 3.

$$D_{Archimedes} = \frac{W_{Dry}}{\left(\frac{W_{Sat} - W_{Susp}}{0.7918}\right)} \quad (3)$$

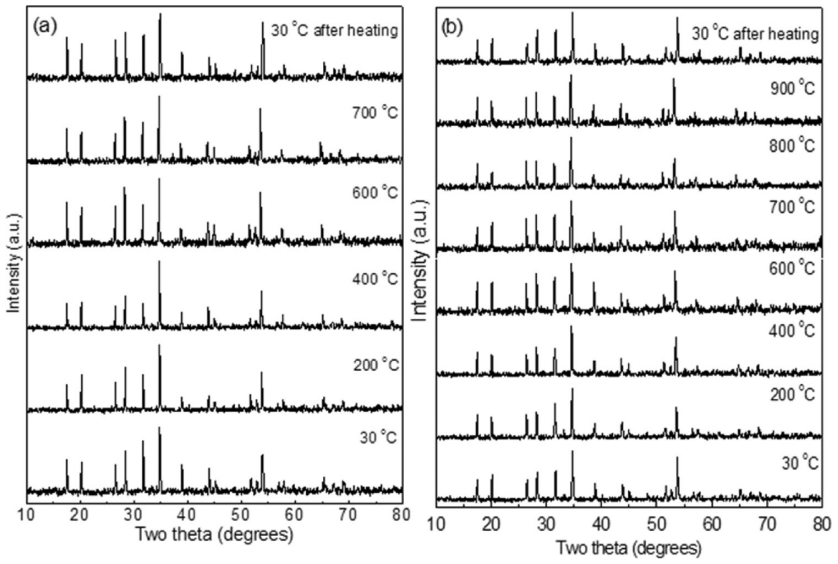

Figure 8. In situ PXRD of $Li_{5+2x}La_3Ta_{2-x}Y_xO_{12}$: (a) x = 0.25 and (b) x = 0.5 showing the thermal stability.

DOI: 10.1021/acs.inorgchem.5b00972
Inorg. Chem. 2015, 54, 6968−6977

The constant 0.7918 in eq 3 is the room-temperature density of methanol (g/cm^3) that was used as the suspension medium in the Archimedes technique. Methanol was used instead of water because garnets tend to exchange Li ions with protons in water, which can affect the accuracy of the density measurements. The potential exchange of Li in methanol has not been considered. The theoretical density (d) was computed from the PXRD data using the expression

$$d = \frac{ZM}{a^3 N_A} \tag{4}$$

where Z is the number of chemical formula per unit cell ($Z = 8$), M is the molar weight of the nominal chemical composition $Li_{5+2x}La_3Ta_{2-x}Y_xO_{12}$, "$a$" is the lattice parameter obtained from PXRD, and N_A is Avogadro's number. As shown in Table 5, the densities of the $x = 0.5$ and 0.75 are significantly greater than the densities obtained for $x = 0.05$, 0.1, 0.2, and 0.25, confirming the direct correlation between the doping level and sinterability in these materials.

3.4. Structural Stability and Chemical Compatibility with Aqueous LiCl Solution. The high structural stability of $Li_{5+2x}La_3Ta_{2-x}Y_xO_{12}$ was studied by in situ PXRD in the temperature range of 30−700 °C, as shown in Figure 8. The thermal expansion coefficient (TEC) of $Li_{5+2x}La_3Ta_{2-x}Y_xO_{12}$ ($x = 0.5$) with temperature was calculated using the lattice parameters derived from in situ PXRD (Figure 8b). The formula used for TEC calculation is shown in eq 5

$$\alpha = \left(\frac{a - a_0}{a_0}\right)\left(\frac{1}{T - T_0}\right) \tag{5}$$

where α, T, and a represent the thermal expansion coefficient, temperature, and lattice parameter at that temperature.[39] The notations a_0 and T_0 represent the corresponding values at room temperature. A thermal expansion coefficient of 7.25×10^{-6} K^{-1} was observed for $Li_6La_3Ta_{1.5}Y_{0.5}O_{12}$.

To determine the stability in aqueous environments, the materials were treated in water, as described in the Experimental Section. The water-treated materials were then studied by variable-temperature PXRD to determine if there were any changes in their structure or stability. Figure 9 shows the corresponding data for the $x = 0.5$ phase and indicates that the water-treated material maintains the cubic structure and is also structurally stable up to 700 °C. We next explored the potential application of $Li_{5+2x}La_3Ta_{2-x}Y_xO_{12}$ as a protective layer for the Li anode in lithium aqueous batteries, where a highly Li$^+$ conductive material that has chemical compatibility with aqueous lithium salts is desired. Therefore, compatibility tests with 1 M aqueous LiCl solution were performed as described in the Experimental Section. The pH change was monitored for 1 week, and results are shown in Figure 10. The change in pH can indicate the exchange of Li$^+$ with proton in

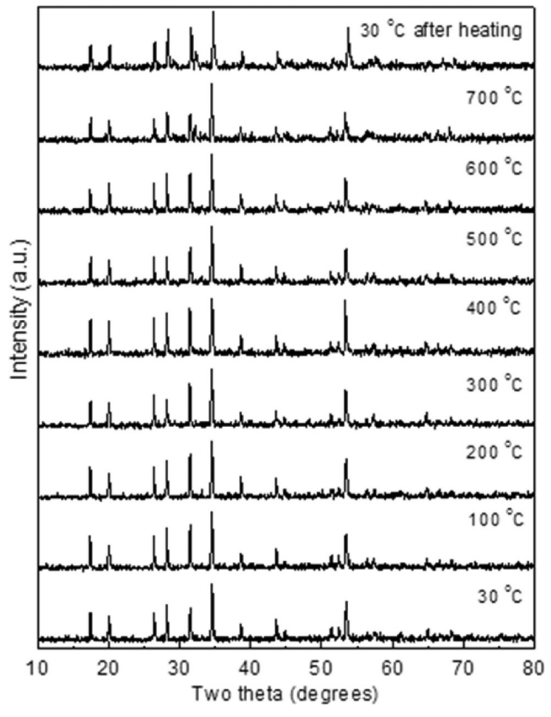

Figure 9. In situ PXRD patterns of water-treated $Li_6La_3Ta_{1.5}Y_{0.5}O_{12}$ showing the structural stability.

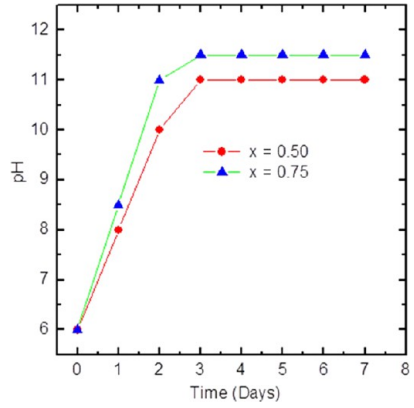

Figure 10. Changes in the pH during the treatment of $Li_{5+2x}La_3Ta_{2-x}Y_xO_{12}$ ($x = 0.50$ and 0.75) in 1 M LiCl solution.

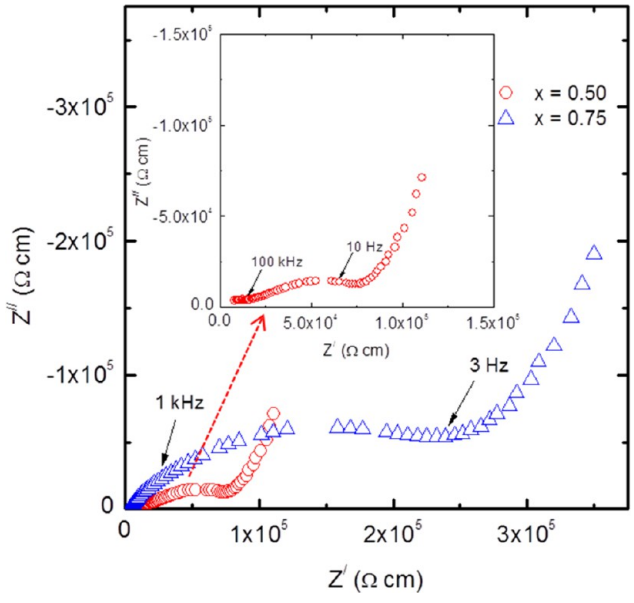

Figure 11. Impedance spectra of $Li_{5+2x}La_3Ta_{2-x}Y_xO_{12}$ ($x = 0.50$ and 0.75) after treatment with 1 M LiCl solution measured at 75 °C. The inset magnifies the data for $x = 0.50$ sample to show the small semicircle at the high-frequency side.

DOI: 10.1021/acs.inorgchem.5b00972
Inorg. Chem. 2015, 54, 6968−6977

$Li_{5+2x}La_3Ta_{2-x}Y_xO_{12}$. An increase in the pH value was observed over the first 2 days, reaching a maximum value of 11−11.5 from an initial value of 6, and remained almost constant for the rest of the week. A similar change in pH was reported in other garnets in water.[40,41]

A comparative impedance study of the aqueous LiCl-treated garnets was also performed. Figure 11 shows the ac impedance plots of LiCl-treated $Li_{5+2x}La_3Ta_{2-x}Y_xO_{12}$ (x = 0.50 and 0.75) measured at 75 °C. The grain-boundary impedance was found to be increasing after the aqueous LiCl treatment in all the cases. As shown in the Arrhenius plot (Figure 5b), the conductivity also drops compared to the as-prepared garnets. This may be partly due to the replacement of Li^+ in the garnet structure with H^+ from the aqueous solution. The pH change during the aqueous LiCl treatment and the presence of −OH peaks in the FTIR spectra (~3500 cm^{-1} for −OH stretching and ~1500 cm^{-1} for −OH bending) as shown in Figure 12 indicate that there was an ion exchange between Li^+ from garnet and H^+ from water during aqueous LiCl treatment.

In order to understand the microstructure, a cross-sectional SEM imaging was also done on the pellets treated in aqueous LiCl, as shown in Figure 13. The SEM data indicated a greater degree of porosity in the samples after aqueous LiCl treatment compared to the untreated materials (Figure 7). The EDX patterns were recorded (Figure 13) in search for chlorine to examine the potential entrapment of LiCl. However, no evidence was found to indicate the presence of a significant amount of chlorine in these samples (Figure 13). Nevertheless, even after the drop in conductivity, the measured values are still significantly greater than the conductivity of the parent undoped compound.[6] The PXRD data of the samples treated after the aqueous LiCl test show that there is no phase change,

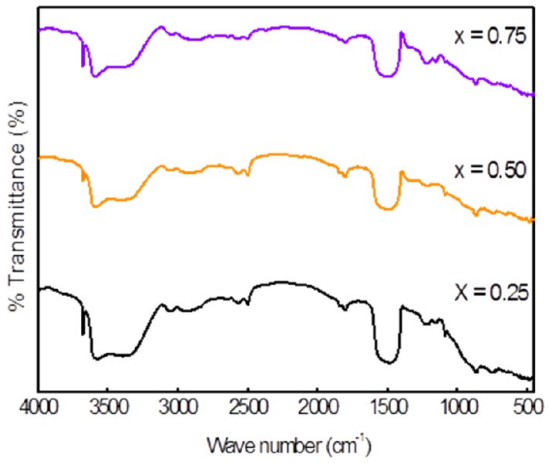

Figure 12. FTIR spectra of water-treated $Li_{5+2x}La_3Ta_{2-x}Y_xO_{12}$ (x = 0.25, 0.5, and 0.75).

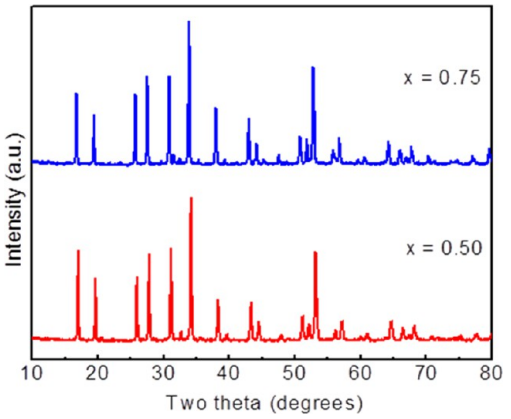

Figure 14. PXRD of $Li_{5+2x}La_3Ta_{2-x}Y_xO_{12}$ (x = 0.5 and 0.75) after reaction with 1 M LiCl solution.

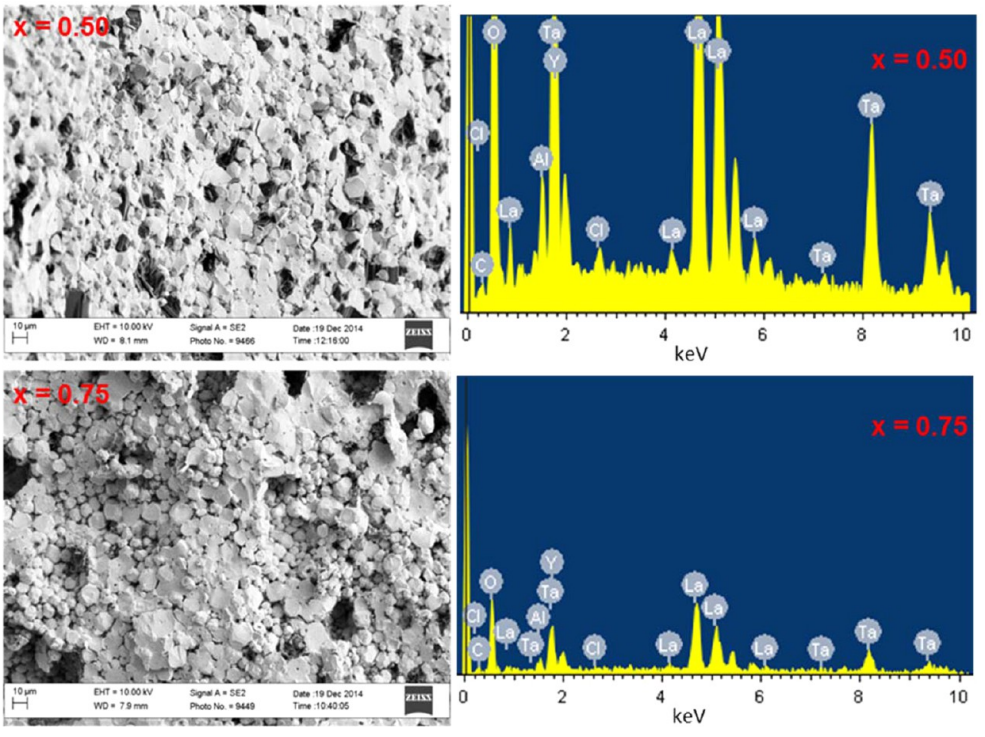

Figure 13. SEM images and EDX results for $Li_{5+2x}La_3Ta_{2-x}Y_xO_{12}$ (x = 0.5 and 0.75) after treatment with 1 M LiCl solution.

DOI: 10.1021/acs.inorgchem.5b00972
Inorg. Chem. 2015, 54, 6968−6977

indicating high structural stability of the garnets, as shown in Figure 14. Thus, the garnet-type $Li_{5+2x}La_3Ta_{2-x}Y_xO_{12}$ materials show a high stability in an aqueous LiCl environment, making them suitable candidates for potential application in Li aqueous batteries.

4. CONCLUSIONS

The garnet-type $Li_{5+2x}La_3Ta_{2-x}Y_xO_{12}$ ($0.05 \leq x \leq 0.75$) was deeply studied to correlate the Y and Li content with conductivity, porosity, and sinterability. ^{7}Li magic-angle spinning NMR shows a direct correlation between the Li content and lithium mobility in these materials, which is consistent with the impedance spectroscopy studies that indicate higher conductivity for materials with greater Li content. The conductivity of these materials over a wide temperature range, from 23 to 325 °C, has also been studied. In addition, with the aid of scanning electron microcopy and Archimedes calculations of porosity and density, a correlation has been established between the sinterability and dopant content, where an increase in sinterability is observed as the Li (and Y) contents increase. Furthermore, stability tests were performed to determine the compatibility of these materials with aqueous LiCl, indicating some decrease in Li conductivity, but very high stability, making $Li_{5+2x}La_3Ta_{2-x}Y_xO_{12}$ a potential candidate for further investigation as a protective layer for lithium electrodes in lithium−air batteries.

AUTHOR INFORMATION

Corresponding Author

*E-mail: vthangad@ucalgary.ca. Phone: 1 (403) 210 8649. Fax: 1 (403) 289 9488.

Present Address

†University of California, Berkeley - Department of Chemistry, Berkeley, California 94709, United States.

Notes

The authors declare no competing financial interest.

ACKNOWLEDGMENTS

The Natural Sciences and Engineering Research Council of Canada (NSERC) supported this work through the Discovery Grants (DG) program.

REFERENCES

(1) Thangadurai, V.; Narayanan, S.; Pinzaru, D. *Chem. Soc. Rev.* **2014**, *43*, 4714−4727.
(2) Thangadurai, V.; Pinzaru, D.; Narayanan, S.; Baral, A. K. *J. Phys. Chem. Lett.* **2015**, *6*, 292−299.
(3) Shimonishi, Y.; Toda, A.; Zhang, T.; Hirano, A.; Imanishi, N.; Yamamoto, O.; Takeda, Y. *Solid State Ionics* **2011**, *183*, 48−53.
(4) Girishkumar, G.; McCloskey, B.; Luntz, A. C.; Swanson, S.; Wilcke, W. *J. Phys. Chem. Lett.* **2010**, *1*, 2193−2203.
(5) Ma, C.; Rangasamy, E.; Liang, C.; Sakamoto, J.; More, L. K.; Chi, M. *Angew. Chem., Int. Ed.* **2014**, *53*, 1−6.
(6) Thangadurai, V.; Kaack, H.; Weppner, W. J. F. *J. Am. Ceram. Soc.* **2003**, *86*, 437−440.
(7) Thangadurai, V.; Weppner, W. *Adv. Funct. Mater.* **2005**, *15*, 107−112.
(8) Thangadurai, V.; Weppner, W. *J. Am. Ceram. Soc.* **2005**, *88*, 411−418.
(9) Murugan, R.; Thangadurai, V.; Weppner, W. *Ionics* **2007**, *13*, 195−203.
(10) O'Callaghan, M. P.; Cussen, E. J. *Solid State Sci.* **2008**, *10*, 390−395.
(11) Xie, H.; Li, Y.; Han, J.; Dong, Y.; Paranthaman, M. P.; Wang, L.; Xu, M.; Gupta, A.; Bi, Z.; Bridges, C. A.; Nakanishi, M.; Sokolov, A. P.; Goodenough, J. B. *J. Electrochem. Soc.* **2012**, *159*, A1148−A1151.
(12) Murugan, R.; Thangadurai, V.; Weppner, W. *Angew. Chem., Int. Ed. Engl.* **2007**, *46*, 7778−7781.
(13) Awaka, J.; Kijima, N.; Hayakawa, H.; Akimoto, J. *J. Solid State Chem.* **2009**, *182*, 2046−2052.
(14) Geiger, C. A.; Alekseev, E.; Lazic, B.; Fisch, M.; Armbruster, T.; Langner, R.; Fechtelkord, M.; Kim, N.; Pettke, T.; Weppner, W. *Inorg. Chem.* **2011**, *50*, 1089−1097.
(15) Buschmann, H.; Dolle, J.; Berendts, S.; Kuhn, A.; Bottke, P.; Wilkening, M.; Heitjans, P.; Senyshyn, A.; Ehrenberg, H.; Lotnyk, A.; Duppel, V.; Kienle, L.; Janek, J. *Phys. Chem. Chem. Phys.* **2011**, *13*, 19378−19392.
(16) Rangasamy, E.; Wolfenstine, J.; Sakamoto, J. *Solid State Ionics* **2012**, *206*, 28−32.
(17) Lee, J.-M.; Kim, T.; Baek, S.-W.; Aihara, Y.; Park, Y.; Kim, Y.-I.; Doo, S.-G. *Solid State Ionics* **2014**, *258*, 13−17.
(18) Wolfenstine, J.; Sakamoto, J.; Allen, J. L. *J. Mater. Sci.* **2012**, *47*, 4428−4431.
(19) Buschmann, H.; Berendts, S.; Mogwitz, B.; Janek, J. *J. Power Sources* **2012**, *206*, 236−244.
(20) Thompson, T.; Wolfenstine, J.; Allen, J. L.; Johannes, M.; Huq, A.; Davida, I. N.; Sakamoto, J. *J. Mater. Chem. A* **2014**, *2*, 13431−13436.
(21) Li, Y.; Han, J.-T.; Wang, C.-A.; Vogel, S. C.; Xie, H.; Xu, M.; Goodenough, J. B. *J. Power Sources* **2012**, *209*, 278−281.
(22) Murugan, R.; Ramakumar, S.; Janani, N. *Electrochem. Commun.* **2011**, *13*, 1373−1375.
(23) Ohta, S.; Kobayashi, T.; Asaoka, T. *J. Power Sources* **2011**, *196*, 3342−3345.
(24) Narayanan, S.; Ramezanipour, F.; Thangadurai, V. *J. Phys. Chem. C* **2012**, *116*, 20154−20162.
(25) Baral, A. K.; Narayanan, S.; Ramezanipour, F.; Thangadurai, V. *Phys. Chem. Chem. Phys.* **2014**, *16*, 11356−11365.
(26) Larson, C. A.; Von Dreele, B. R. *General Structure Analysis System*; Los Alamos National Laboratory Report LAUR 86-748; The Regents of the University of California: Oakland, CA, 1994.
(27) Toby, B. H. *J. Appl. Crystallogr.* **2001**, *34*, 210−213.
(28) Shannon, R. D. *Acta Crystallogr.* **1976**, *A32*, 751−767.
(29) Muller, O.; Roy, R. *The Major Ternary Structural Families*; Crystal Chemistry of Non-Metallic Materials; Springer-Verlag: New York, 1974; pp 177−178.
(30) Cussen, E. J. *Chem. Commun.* **2006**, 412−413.
(31) O'Callaghan, M. P.; Cussen, E. J. *Chem. Commun.* **2007**, 2048−2050.
(32) Cussen, E. J. *J. Mater. Chem.* **2010**, *20*, 5167.
(33) Narayanan, S.; Thangadurai, V. *J. Power Sources* **2011**, *196*, 8085−8090.
(34) Irvine, J. T. S.; Sinclair, D. C.; West, A. R. *Adv. Mater.* **1990**, *2*, 132−138.
(35) Dumon, A.; Huang, M.; Shen, Y.; Nan, C.-W. *Solid State Ionics* **2013**, *243*, 36−41.
(36) Narayanan, S.; Epp, V.; Wilkening, M.; Thangadurai, V. *RSC Adv.* **2012**, *2*, 2553.
(37) Rettenwander, D.; Langer, J.; Schmidt, W.; Arrer, C.; Harris, K. J.; Terskikh, V.; Goward, G. R.; Wilkening, M.; Amthauer, G. *Chem. Mater.* **2015**, *27*, 3135−3142.
(38) Gore, M. C.; White, O. J.; Wachsman, D. E.; Thangadurai, V. *J. Mater. Chem. A* **2014**, *2*, 2363−2373.
(39) Handal, H. T.; Thangadurai, V. *J. Power Sources* **2013**, *243*, 458−471.
(40) Truong, L.; Thangadurai, V. *Chem. Mater.* **2011**, *23*, 3970−3977.
(41) Liu, C.; Rui, K.; Shen, C.; Badding, M. E.; Zhang, G.; Wen, Z. *J. Power Sources* **2015**, *282*, 286−293.

DOI: 10.1021/acs.inorgchem.5b00972
Inorg. Chem. 2015, 54, 6968−6977